



Thickness-dependent carrier lifetime and mobility for MAPbBr₃ single crystals



J. Xing^{a, b}, Y. Zou^{a, b}, C. Zhao^{a, b}, Z. Yu^{a, b}, Y. Shan^{a, b}, W. Kong^{a, b}, X. Zheng^{a, b}, X. Li^{a, b}, W. Yu^{a, b, *}, C. Guo^{a, c, **}

^a The Guo Photonics Laboratory, State Key Laboratory of Applied Optics, Changchun Institute of Optics, Fine Mechanics and Physics, Chinese Academy of Sciences, Changchun, 130033, PR China

^b University of Chinese Academy of Sciences, Beijing, 100049, PR China

^c The Institute of Optics, University of Rochester, NY, 14627, USA

ARTICLE INFO

Article history:

Received 2 April 2020

Received in revised form

11 May 2020

Accepted 21 May 2020

Available online 12 June 2020

Keywords:

Dynamics

Carrier mobility

Perovskite

Thickness

Transport

ABSTRACT

Carrier transfer is a key process for perovskite-based photoelectric conversion. It has a close relationship with grain boundaries, grain size, and contact layers. Understanding this relationship is of great significance for revealing the inherent characteristics of perovskite materials and for devices optimization. However, the dependence of carrier transfer characteristics (including carrier lifetime and mobility) on thickness is less studied, although which is a key issue for almost all perovskite material devices. Here we find that as the thickness of MAPbBr₃ perovskite single crystal (PSC) increases from 1.47 μm to 10.55 μm, the carrier lifetime of MAPbBr₃ decreases from 70 ns to 30 ns, and the carrier mobility decreases from 97 cm² V⁻¹ s⁻¹ to 57 cm² V⁻¹ s⁻¹, but they become constant in very thick samples. In addition, it was found that as the crystal thickness increased from 1.47 μm to 10.55 μm, the surface layer range gradually increased from 12 nm to 31 nm. The surface recombination velocity and surface defect (trap) density further confirmed that the thin PSC exhibited a small surface layer range. Finally, a three-layer carrier transmission model of PSC is proposed. This research provides guidance for the optimal design of PSC optoelectronic devices.

© 2020 Elsevier Ltd. All rights reserved.

1. Introduction

Metal halide perovskite has achieved a wide range of applications in solar cells [1–3], photodetectors [4,5], field effect transistors [6–8], lasers [9], and light-emitting diodes [10–12], which are closely related to its good absorption characteristics and effective carrier transport properties [13–16]. To explore the influencing factors and mechanism of perovskite carrier transport performance is of great significance for unveiling how perovskite materials work and for developing high-performance devices. Poor carrier transport characteristics, e.g. short carrier lifetime and low mobility, which indicates a large number of carrier recombination happening, will inevitably reduce the performance and the lifetime of perovskite optoelectronic devices. Some previous studies have

shown that carrier transport is related to multiple factors such as grain boundary, grain size, stoichiometry, and so on [13,16]. For example, Ginger et al. group reports [17] that the carrier lifetime and photoluminescence (PL) intensity of perovskite polycrystalline thin films change with variations in grain size. The grain boundaries are dimmer and exhibit faster non-radiative decay than the surrounding grains [17]. Recombination losses at the interfaces between the perovskite and the electron/hole transport layer may also have a significant effect on carrier transport. To facilitate the carrier transport, pioneering researchers have tried to increase the grain size of the perovskite and/or the method of surface passivation treatment and have achieved success to some extent [13,18,19]. Some passivation molecules have been tried, such as potassium iodide [20] and guanidine bromide [21], and have been approved successfully in passivating surface defects. These molecules may react with the uncoordinated dangling bonds of the surface atoms and quench the photoexcited carriers [22].

Among the various morphologies of perovskites that have been synthesized, such as polycrystalline thin films [1,23], quantum dots

* Corresponding author.

** Corresponding author.

E-mail addresses: weili.yu@ciomp.ac.cn (W. Yu), guo@optics.rochester.edu (C. Guo).

[10], nanowires [24–26], platelets [27,28], single crystal bulks (SCBKs) [4,29,30], and single crystals thin films (SCTFs) [31,32], perovskite single crystal (PSCs, including SCBK and SCTFs) with larger grains and fewer grain boundaries can effectively transport carriers, and therefore it is the ideal material for studying the intrinsic transport properties of perovskites and the preparation of electronic devices [18,31,32]. However, research on transport property and application of large single crystals, are still limited. Some basic questions such as whether the carrier lifetime and mobility are constant or not and how the transport property evolves with crystal thickness are still open questions.

In this article, by measuring the carrier transport property and defects density of MAPbBr₃ single crystals (MPB SCs) samples, we explored the dependence of perovskite carrier lifetime and mobility on thickness. First, controlled thickness (from 1.47 μm to 10.55 μm) MPB SCTFs are synthesized by confining the space between two slides and adjusting precursor solution concentration. Then, through time-resolved photoluminescence (TRPL) and space charge limited current (SCLC) measurements, the carrier average lifetime and carrier mobility of MPB SCs with various thickness are monitored, and the dependence of carrier lifetime and mobility on crystal thickness are extracted. Furthermore, the surface recombination velocity and surface defects (trap) density are calculated, which give a straightforward explanation of the evolution results mentioned previously. Finally, a three-layer carrier transfer model of MPB SCs is proposed to describe the thickness-dependent carrier transport property evolution process, which may work not only for MAPbBr₃ but also for other perovskites such as MAPbCl₃, FAPbI₃, and so on.

2. Results and discussion

2.1. Synthesis and characterization of MPB SCs with different thickness

MPB SCTFs with controlled thickness were synthesized through an improved one-step space-limited crystal incubation process referring to previous reports [6,32–34]. As shown in Fig. 1a, 10 μL

MAPbBr₃ precursor solution with various concentration (from 10 mM to 1000 mM) was dropped on hydrophobic-treated silicon wafer, and then it was covered by hydrophobic-treated coverslip. After two days, the MPB SCTF was achieved as the solvent slowly evaporated in air at room temperature. By tuning the precursor solution concentration, MPB SCTFs with various thicknesses can be achieved. The relationship between concentration of precursor solutions and thickness of MPB SCTFs is shown in Fig. 1b. The thickness of MPB SCTFs first shows a large growth slope from 10 mM to 100 mM and then increases slightly after 100 mM. The variation of MPB SCTFs thickness still shows the same trace after changing substrate to be a hydrophobic-treated glass. This indicates that thickness tuning method is substrate independent, which is consistent with previous report [34]. The detailed information of the MPB SCTFs thickness with different precursor solution concentration on silicon wafer and glass are summarized in Supplementary Table S1 and Table S2.

Fig. 1c–n shows the optical photographs and three-dimensional (3D) pseudo color plots of MPB SCTFs with different thicknesses. The MPB SCTFs are submillimeter-sized in length and width with a uniform surface. The orange color becomes gradually deepened as thickness increases from 1.47 μm to 10.55 μm. The detailed thickness information and three-dimensional height results of the MPB SCTFs are shown in Supplementary Fig. S1. A scanning electron microscope (SEM) image of the MPB SCTFs in Supplementary Fig. S2 shows a smooth surface without any grain boundary. The energy dispersive spectrometry (EDS) mapping results in Supplementary Figs. S2b–g show uniform elemental distributions of bromide, lead, carbon, nitrogen from MPB SCTF, and oxygen, as well as silicon from silicon substrate. The clear and distinct elemental boundaries between MPB SCTF and substrate further confirm the high crystallinity, and the peak distribution of each element are presented in Supplementary Fig. S2h. The X-ray diffraction (XRD) results of MPB SCTF, MPB SCBK, MPB SC powder, PbBr₂ and methylammonium bromide (MABr) are shown in Supplementary Fig. S3. The MPB SCBK is synthesized by the improved inverse temperature crystallization (ITC) method as our previous report [35]. XRD results of MPB SCTF, MPB SCBK, and MPB

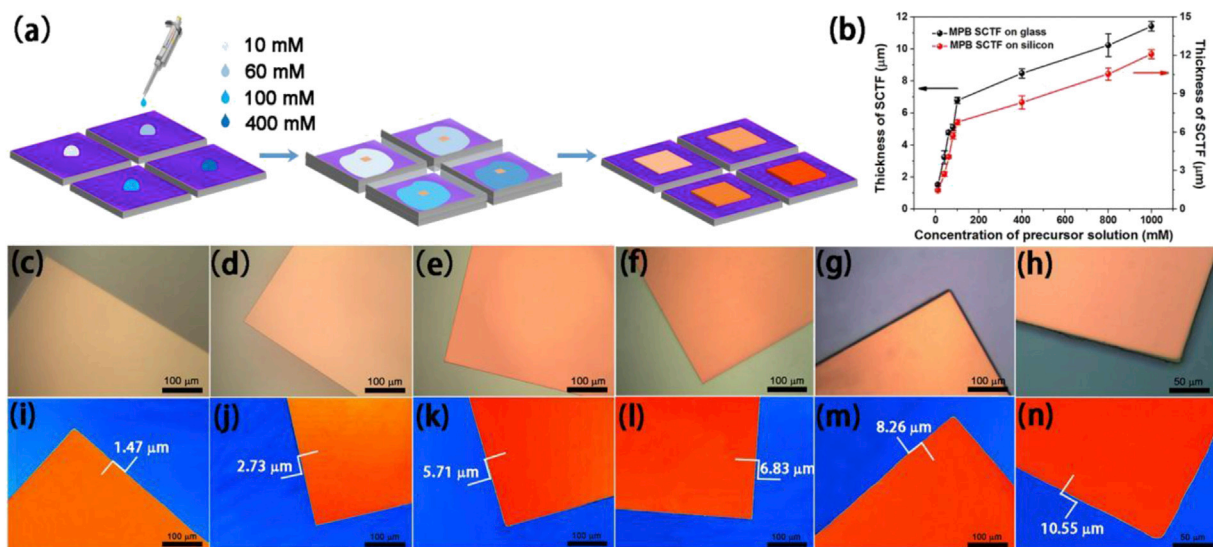


Fig. 1. One-step space-limited growth method for MPB SCTFs. (a) Schematic illustration of one-step space-limited growth method. First, different concentration of MAPbBr₃ precursor solution was dropped on hydrophobic-treated silicon wafer. Second, the precursor solution was covered by hydrophobic-treated coverslip. Final, MPB SCTFs with different thickness were obtained after solution evaporation. (b) The relationship between precursor solution concentration and thickness of MPB SCTFs on silicon and glass substrate. (c–h) Optical photographs of MPB SCTFs with different thicknesses (1.47 μm, 2.73 μm, 5.71 μm, 6.83 μm, 8.26 μm, 10.55 μm). (i–n) Three-dimensional (3D) pseudo color plots of MPB SCTFs with different thickness. (For interpretation of the references to color in this figure legend, the reader is referred to the Web version of this article.) SCTFs, single crystals thin films.

SC powder all show a cubic structure, which is consistent with previous reports [36]. Moreover, the characteristic peaks of PbBr_2 and MABr disappear in MPB SCTF and MPB SCBK, indicating that MABr and PbBr_2 have been completely converted into MPB SCTF and MPB SCBK. Supplementary Fig. S4 shows Raman spectrum of MPB SCBK and MPB SCTF. The characteristic peaks in MPB SCBK and MPB SCTF show same positions (55, 324, 918, 969, 1250, 1477, 1586, and 2966 cm^{-1}) [37], which also indicates that MPB SCBK and MPB SCTFs own same crystalline structure. The absorption spectrum of MPB SCTFs in Supplementary Fig. S5a shows that the absorbance will increase with increase in crystal thickness. Besides, absorption cutoff wavelength shows a gradual red shift with MPB SCTFs getting thick in Supplementary Fig. S5b, which is consistent with previous calculations [2]. All characterizations indicate that the improved one-step space-limited growth method is simple and easy to control MPB SCTFs thickness with a high quality.

2.2. Steady state PL and TRPL of MPB SCs with different thickness.

The light penetration in perovskite materials is constrained within a few hundred nanometers due to the large absorption coefficients [32,38]. In this region, the transfer and recombination of carriers are still susceptible to the influence from the surface [32,38]. To explore thickness' effects, especially the influence from surface, on PL intensity, steady state PL of MPB SCTFs with different thickness was measured in air at room temperature under 473 nm laser. For each thickness, five samples were measured, and the associated PL intensity results are shown in Supplementary Fig. S6. The PL intensity varies in a narrow range with no obvious peak shift at same thickness, which proves the universality and repeatability of the growth method. In Fig. 2a, PL intensity goes upward without obvious peak shift as thickness increasing. The inset shows a linear correlation between maximum PL intensity and MPB SCTFs thickness. A related report shows that the surface band structure of single crystal closely resembles that of the polycrystalline thin films [38], which indicates that the diffusion of carriers in the surface is limited compared with bulk region. Thereby more charged carriers will be promoted to generate fluorescence in surface layer, whereas more charged carriers tend to diffuse freely in the bulk region,

which showing different PL intensity between surface layer and bulk region in PSCs. Thus, the positive correlation between maximum PL intensity and MPB SCTFs thickness in Fig. 2a indicates that the surface layer region will shows a gradual expansion with MPB SCTFs' thickness increasing, which is an unreported but very instructive phenomenon.

To explore the variation of carrier lifetime and confirm the gradual changes of surface layer in MPB SCs with different thickness, we carried out TRPL to measure the PL decay under 532 nm ps laser in air. For each thickness, five samples were measured for comprehensiveness and accuracy. Supplementary Figs. S7–S15 show the PL decay traces of MPB SCs with different thickness. Each PL decay trace can be fitted with tri-exponential decay function and the carrier lifetime in three decay processes (including fast, middle and slow process) can be obtained [39]. The carrier lifetimes (τ_1, τ_2, τ_3), fractional contributions (f_1, f_2, f_3) and calculated average carrier lifetime ($\tau_{\text{ave}} = \tau_1 f_1 + \tau_2 f_2 + \tau_3 f_3$) [40] are shown in Supplementary Tables S3–S11. The dependence of τ_{ave} with MPB SCs thickness is shown in Fig. 2b. With thickness increasing from $1.47 \mu\text{m}$ to $10.55 \mu\text{m}$, the τ_{ave} exhibits a thickness-dependent single exponential decay (attenuated from 70 ns to 30 ns) and then remains stable (maintained at around 30 ns) when the thickness ranges from $10.55 \mu\text{m}$ to $3500 \mu\text{m}$.

It is necessary to discuss the relationships between the parameters of $\tau_1, \tau_2, \tau_3, f_1, f_2, f_3$ and MPB SCs thickness. The short lifetime (τ_1) corresponds to exciton recombination occurring in surface layer; the middle lifetime (τ_2) corresponds to electron-hole pair recombination occurring in surface-bulk transition region, and the long lifetime (τ_3) corresponds to free carrier recombination occurring in bulk region of MPB SCs [41]. As shown in Fig. 2c, with thickness increasing, τ_1, τ_2, τ_3 reduce first, and then become stable (τ_1 changes from 8 ns to 2 ns, τ_2 decreases from 27 ns to 12 ns, and τ_3 falls from 100 ns to 70 ns). It is noteworthy that the turning point from decay to stable is at $10.55 \mu\text{m}$, which is consistent with τ_{ave} .

The variations of fractional contribution (f_1, f_2, f_3) with different thicknesses are shown in Fig. 2d. The f_1, f_2, f_3 represent the contributions of τ_1, τ_2, τ_3 to τ_{ave} and show varying trends with thickness [42]. The f_1 and f_2 both exhibit a slow-growth tendency first and then become stable as thickness increases. However, the f_3

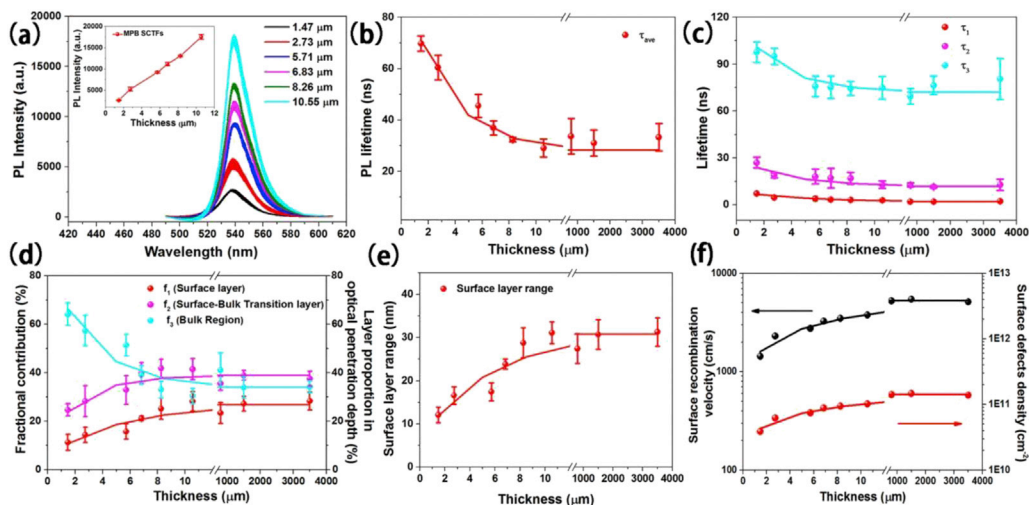


Fig. 2. Steady state photoluminescence (PL) and time-resolved photoluminescence (TRPL) characterization. (a) Steady state PL of MPB SCTFs with different thicknesses. The measurement is under 473 nm laser in air at room temperature. (b) PL average lifetime of MPB SCs with different thicknesses. The measurement is under 532 nm laser in air at room temperature. (c) The variation of three decay process lifetimes (τ_1, τ_2, τ_3) in MPB SCs with different thicknesses. (d) The variation of fractional contribution (f_1, f_2, f_3) in three decay process and three layer (surface layer, surface-bulk transition layer, and bulk region) proportion in optical penetration depth of MPB SCs with different thicknesses. (e) The variation of surface layer range in MPB SCs with different thicknesses. (f) The variation of surface recombination velocity and surface defects density in MPB SCs, single crystals thin films.

shows single exponential decay. This indicates that as thickness increases, the fractional contribution of surface layer and surface-bulk transition layer increases gradually, as well as their influence on τ_{ave} . Conversely, the fractional contribution of bulk region reduces. Therefore, the fractional contribution (f_1, f_2, f_3) can be approximated as the proportion of each layer in optical penetration depth [40]. Thus, the changing contribution of each layer to τ_{ave} can also be expressed in Fig. 2d, [42]. The absorption coefficient (α) of MPB SCs is around $88,000 \text{ cm}^{-1}$ at 532 nm and the optical penetration depth (δ) at 532 nm can be calculated to be 113 nm [32]. Based on this assumption, the surface layer range with different thickness can be calculated, and the results are shown in Fig. 2e. It shows that the surface layer first gradually increase from 12 nm to 31 nm and then maintains stable when crystal thickness is larger than 10.55 μm .

Exploring the variation of surface layer is helpful to understand carrier transfer behavior. Surface recombination velocity and surface defects density are important parameters for judging surface properties. These two parameters can be calculated according to the following equations: [38,43]

$$1/\tau_S = 1/\tau_B + \alpha S \quad (1)$$

$$S = \sigma \nu_{th} N_t \quad (2)$$

where τ_S is surface lifetime (τ_1), τ_B is bulk lifetime (τ_3), α is absorption coefficient, S is surface recombination velocity, σ is a typical recombination surface cross section in semiconductors ($\approx 10^{-15} \text{ cm}^{-2}$), ν_{th} is the carrier thermal velocity ($\approx 3.7 \times 10^7 \text{ cm s}^{-1}$), and N_t can be considered as the surface defects density. As shown in Fig. 2f, both S and N_t show similar trend with the surface layer range in Fig. 2e. Assuming the defects are evenly distributed in the surface layer [44], the calculated S and N_t displays the gradual expanding of surface layer range with crystal thickness increasing. This indicates that carrier transfer in MPB SCs is efficient and better photoelectric performance can be achieved in thin crystal owing to narrow surface layer range. The thickness-dependent fluorescence characteristics and surface layer range will be helpful for the optimization of photovoltaic devices based on MPB SCs.

2.3. J_D - V characterization and carrier mobility of MPB SCs with different thickness

It is worthwhile mentioning that surface carrier mobility of MPB SCs is related to surface layer properties [43]. To investigate the inherent reason of thickness-dependent fluorescence characteristics, an Au/MPB SCs/Au device is prepared to measure the surface carrier mobility through horizontal space charge limited current (SCLC) method, and the schematic diagram is shown in Fig. 3a.

100 nm thick gold electrode is deposited on MPB SCs, with the length of 480 μm and width of 110 μm between two electrodes. The optical image of the device is show in Supplementary Fig. S16. Once the depletion width, in which the free carrier density shows uniform distribution, is larger than the optical penetration depth, the carrier mobility obtained from SCLC can be used to characterize the surface layer properties [43]. The depletion width (W) of Au/MPB SCs Schottky junction can be calculated [45]:

$$W = \sqrt{\frac{2\epsilon\epsilon_0(\phi_{bi} - V)}{qN}} \quad (3)$$

where ϵ is the static dielectric constant of MPB SCs (around 4.8) [46], ϵ_0 is the permittivity of free space, ϕ_{bi} is the built-in potential of Au/MPB SCs schottky junction and is equivalent to the voltage (around 0.03 V) at which the photocurrent ($J_{Light} - J_{Dark}$) becomes zero [47] as shown in Supplementary Fig. S17a, V is the applied bias, and N is the free carrier density at the edge of the depletion layer (around $7.15 \times 10^{13} \text{ cm}^{-3}$) [31]. The calculated depletion width changes with free carrier density and applied voltage is shown in Supplementary Fig. S17b. Even with a small applied bias of 1 V, the depletion width is greater than 300 nm, much larger than the optical penetration depth (about 113 nm) at 532 nm. It indicates that horizontal SCLC is an effective method to characterize the surface layer properties of MPB SCs.

The dark current J_D - V traces for each thickness MPB SCs are shown in Fig. 3b. It can be observed that the trap-filled limit voltage (V_{TFL}) increases gradually as MPB SCs becoming thicker. The detailed information of J_D - V traces with different crystal thickness is shown in Supplementary Figs. S18–26. In the J_D - V trace, it shows three different regimes: ohmic regime (red line) at low bias; trap-filled regime (black line) with a starting point (V_{TFL}), which indicates all the traps are filled at this bias; Child regime (blue line) at high bias. The trap density (n_t) and carrier mobility (μ) could be calculated based on the following equations: [48,49]

$$V_{TFL} = en_t L^2 / (2\epsilon\epsilon_0) \quad (4)$$

$$J_D = 9\epsilon\epsilon_0 \mu V_b^2 / (8L^3) \quad (5)$$

where L is the distance between two electrodes (110 μm), ϵ is relative dielectric constant of MPB SCs (about 4.8) [46], ϵ_0 is the vacuum permittivity, J_D is the current density at the applied voltage V_b , which is the bias between trap-filled regime and Child regime. The calculated trap density and carrier mobility for each thickness are shown in Supplementary Figs. S18–26, and their relationship with MPB SCs thickness is shown in Fig. 3c. The trap density from SCLC shows the same trend as surface defects density (Fig. 2f) and

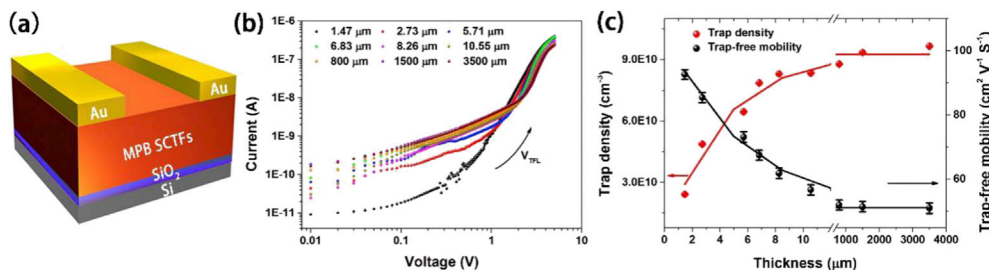


Fig. 3. J_D - V characterization, trap density, trap-free carrier mobility of MPB SCs with different thickness in dark at room temperature. (a) Schematic diagram of MPB SCTFs device. (b) Characteristic J_D - V trace of MPB SCs with different thicknesses. (c) The trap density and trap-free carrier mobility of MPB SCs with different thickness. SCTFs, single crystals thin films.

surface layer range, and the carrier mobility also exhibits a single exponential decay (attenuated from $97 \text{ cm}^2 \text{ V}^{-1} \text{ S}^{-1}$ to $57 \text{ cm}^2 \text{ V}^{-1} \text{ S}^{-1}$) consistent with τ_{ave} , which confirm that the surface layer gradually expands with MPB SCs thickness. It is worth noting that defect density and carrier mobility are stable after when thickness is higher than $10.55 \mu\text{m}$, while showing a significant thickness dependence when it is less than that.

2.4. The mechanism of carrier transfer in MPB SCs

We thus propose a three-layer carrier transfer model in MPB SCs for elaborating the carrier transfer process. Fig. 4a shows the carrier transfer process in surface layer, surface-bulk transition layer and bulk region in MPB SCs after single photon absorption [43,50]. First, when excitation laser (532 nm) is focused on MPB SCs surface, the electron in valence band (V_B) will absorb energy and jumps to conduction band (C_B), producing initial photoexcitation carriers [40]. Then the carriers in surface layer will gradually diffuse into bulk region with time. Because recombination process occurs simultaneously with carrier diffusion motion, some carriers occur exciton recombination in surface layer, and the carrier lifetime in this process is short lifetime τ_1 (surface lifetime τ_s) [29]. Owing to inevitable surface defects (such as uncoordinated dangling bonds of surface atoms, ion deletion, and so on), much more carriers will be trapped and occur non-radiative recombination in surface layer, eventually generating heats instead of fluorescence [51,52]. Then, the remaining carriers diffuse into surface-bulk transition layer, and emit fluorescence under electron-hole pairs recombination, which corresponds to middle lifetime τ_2 [52]. There is still a portion of electron-hole pairs that undergoes non-radiative recombination after being trapped in this region owing to unavoidable volume defects (such as lead vacancies, MA-lead antisite substitutions) [53]. Finally, some carriers with a longer diffusion distance become free carriers and come into bulk region, with emitting fluorescence through band to band recombination. The bulk region in MPB SCs

has a very low defects density compared with surface layer, and therefore the radiative recombination in bulk region owns a long lifetime τ_3 (bulk lifetime) [54]. The properties of MPB SCs surface are different from those in bulk is mainly due to the electric field generated near MPB SCs surface via spontaneous separation of halides ions and vacancies [29]. Especially, the ions and vacancies are more concentrated on MPB SCs surface layer compared with bulk region. It indicates that efficient carrier transfer and long carrier lifetime in MPB SCs can be achieved through weakening the influence of surface layer.

The aforementioned variation of surface layer range in MPB SCs is presented in Fig. 4b. The excitation laser is focused on MPB SCs surface, and the mainly influenced region (green focus) is concentrated in the range of optical penetration depth (around 113 nm) from surface to bulk. As crystal thickness increasing from $1.47 \mu\text{m}$ to $10.55 \mu\text{m}$, the surface layer (deep color layer) slowly expands from 12 nm to 31 nm. When MPB SCTFs thickness is larger than $10.55 \mu\text{m}$ and goes up to $800 \mu\text{m}$, $1500 \mu\text{m}$ and $3500 \mu\text{m}$, the surface layer range remains stable around 31 nm. The surface defects (trap) density from TRPL and SCLC measurement proved that with MPB SCTFs thickness increasing from $1.47 \mu\text{m}$ to $10.55 \mu\text{m}$, the halides ions and vacancies density gradually increase, which leads to an enhancement of electric field generated near surface layer. Owing to halide vacancies controlling the properties of surface [29], the surface layer range shows slowly expanding with MPB SCTFs thickness increasing. After MPB SCs thickness larger than $10.55 \mu\text{m}$, the electric field generated near-surface layer may become steady and lead surface layer range remaining stable [29]. This indicates that the MPB SCTFs will show MPB SCBK properties after a turning point around $10.55 \mu\text{m}$, and the carrier lifetime and carrier mobility show significant thickness dependence in MPB SCTFs with thickness less than $10.55 \mu\text{m}$.

3. Conclusion

In summary, we demonstrated the dependence of carrier lifetime and mobility on perovskite single crystal thickness. The carrier lifetime reduces from 70 ns to 30 ns and carrier mobility decreases from $97 \text{ cm}^2 \text{ V}^{-1} \text{ S}^{-1}$ to $57 \text{ cm}^2 \text{ V}^{-1} \text{ S}^{-1}$ in MPB SCs as the crystal thickness increasing from $1.47 \mu\text{m}$ to $10.55 \mu\text{m}$, and both parameters become stable after that. The evolution mechanism may be attributed to the variation of surface layer thickness with the increasing of crystal thickness. Besides, the calculated surface recombination velocity and surface defects (trap) density also show crystal thickness dependence, which explains the trend and characteristic of carrier lifetime. Finally, a three-layer carrier transfer model of MPB SCs was proposed to clarify the dynamic carrier transport properties in MPB SCs. This work provides guidance for the further studies of carrier transfer and optimization strategies for optoelectronics based on perovskites.

4. Materials and methods

4.1. Materials

The lead bromide (PbBr_2) (99%, Aladdin), N, N-Dimethylformamide (DMF) (99.5%, Aladdin), methylamine solution (40% aqueous solution, Aladdin) and trichloro octadecyl silane (>85.0% [GC], Aladdin) were purchased from Aladdin. The hydrobromic acid (HBr) (40% aqueous solution), ethanol absolute, and diethyl ether were purchased from Sinopharm Chemical Reagent Co., Ltd. All materials were used as received without further purification.

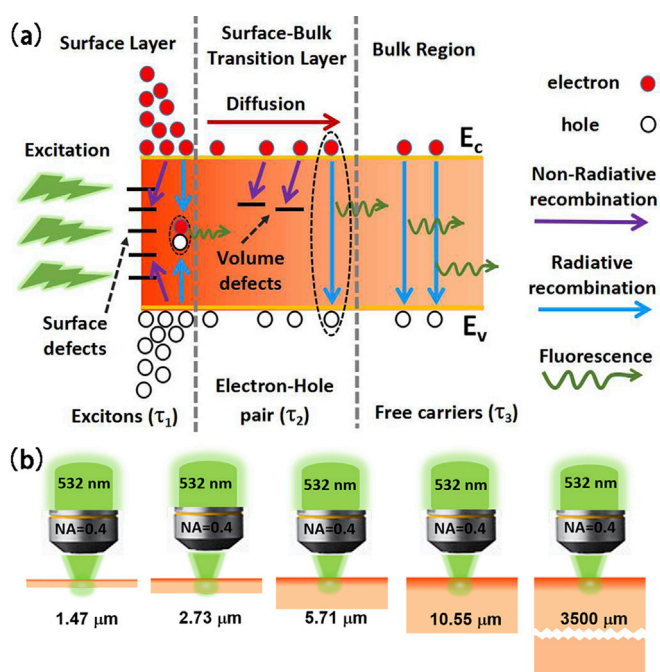


Fig. 4. The mechanism of carrier transfer and surface layer evolution in MPB SCs. (a) Schematic diagram of three-layer carrier transfer model in MPB SCs after single photon absorption. (b) Schematic diagram of gradually expanding of surface layer in MPB SCs with different thickness.

4.2. Synthesis MABr

The MABr was synthesized through the reaction of HBr acid solution (44 mL) with methylamine solution (30 mL) in an ice bath for 2 h with stirring. Then the solvent was removed to recover the white powder by rotary evaporation at 60 °C. Then, the white powder (MABr) was recrystallized from ethanol absolute and diethyl ether for three times. Finally, the MABr was collected by filtration and dried at 60 °C in a vacuum at least 12 h.

4.3. Synthesis of MPB SCTFs

The substrate (Si/SiO₂ and glass) and coverslip (24 mm × 24 mm) were cleaned by rinsing with deionized water, ethanol, acetone, isopropanol in turn. After dried with N₂ gas, the substrates and coverslip were exposed to UV-O₃ for 20 min. Then, the substrates and coverslip were immersed in hexane and trichloro octadecyl silane mixture (500:1) to produce a hydrophobic surface. Then, the substrates and coverslip were rinsed with acetone for 30 s and dried with N₂ gas. Thereafter, 10 μL MAPbBr₃ precursor solution with different concentration was dropped on the hydrophobic-treated substrate, and it was covered by hydrophobic-treated coverslip. MPB SCTFs were achieved at room temperature for 2 days as the solvent slowly evaporates.

4.4. Synthesis of MAPbBr₃ SCBK

MPB SCBK was grown from 1.5 M solution containing PbBr₂ (1.5 mmol) and MABr (1.5 mmol) in DMF (10 mL) using the ITC method in accordance with our previous report [30]. First, the MAPbBr₃ precursor solution was prepared at room temperature by mixing these two materials completely. Then it was filtered by a PTFE filter (0.22 μm) for a clear solution. Then, the clear solution was undisturbed kept in an oil bath with gradually raising oil temperature from 25 °C to 75 °C for MPB SCBK growth. Finally, MPB SCBK with 800 μm, 1500 μm, and 3500 μm thickness were obtained by controlling the growth time from 1 h to 3 h.

4.5. Characterization of MAPbBr₃ single crystal

Three-dimensional (3D) pseudo color plots of MPB SCTFs were obtained by using a KEYENCE VK-X200 3D laser scanning microscope. The SEM image and EDS mapping results of MPB SCTFs were measured from a Phenom Pro-X. The XRD measurement was performed by using a BRUKER D8 FOCUS. Raman spectrum measurement was conducted by using a HORIBA Scientific Raman spectrometer. The absorption spectrum were recorded from an Agilent Cary 5000. Steady state PL spectrum was obtained by a HORIBA Scientific Raman Spectrometer with 2.55 mW cm⁻² laser intensity at 473 nm. TRPL: The MPB SCTFs and MPB SCBKs were measured from home-built confocal microscope (with objective lens N.A. = 0.4) using a pulsed supercontinuum laser (OYSL Photonics, SC-Pro, 150 ps pulse lengths) at 2 MHz repetition rate. The pump wavelength was 532 nm and laser power density is 6312 μW cm⁻² with laser lines filter (Semrock). The Pump scatter light from pump laser to the detector was filtered out using long-pass filter with a 532 nm edge (Semrock). The PL was detected by SPCM-AQRH Single Photon Counting Module (SPCM-AQRH-15, Excelitas Technologies) and the lifetime module was TimeHarp 260 P (PicoQuant). The J-V characteristic curves of MPB SCs with different thickness were obtained by using a Keithley 4200A semiconductor parametric analyzer (Tektronix) and a C-100 probe station from TPSi Company in air at room temperature.

Data availability

The data that support the findings of this study are available from the corresponding authors upon reasonable request.

Credit author statement

Jun Xing: Conceptualization, Methodology, Writing - original draft; **Yuting Zou:** Resources, Data curation; **Chen Zhao:** Resources; **Zhi Yu:** Data curation; **Yuwei Shan:** Formal analysis; **Wenchi Kong:** Resources; **Xin Zheng:** Validation; **Xiuyun Li:** Validation; **Weili Yu:** Conceptualization, Methodology, Writing - review & editing, Visualization; **Chunlei Guo:** Supervision, Project administration, Funding acquisition

Declaration of competing interest

The authors declare no conflict of interest.

Acknowledgements

This work was supported by the National Key Research and Development Program of China (2018YFB1107202, 2017YFB1104700), the Natural Science Foundation of China (NSFC, 91750205, 61774155, 51102107), K. C. Wong Education Foundation (GJTD-2018-08) and the Open Project of State Key Laboratory of Supramolecular Structure and Materials (SKLSSM202034).

Appendix A. Supplementary data

Supplementary data to this article can be found online at <https://doi.org/10.1016/j.mtphys.2020.100240>.

References

- [1] H.H. Fang, et al., Photoexcitation dynamics in solution-processed formamidinium lead iodide perovskite thin films for solar cell applications, *Light Sci. Appl.* 5 (2016): e16056.
- [2] Z. Chen, et al., Thin single crystal perovskite solar cells to harvest below-bandgap light absorption, *Nat. Commun.* 8 (2017) 1890–1896.
- [3] Q.F. Han, et al., High-performance perovskite/Cu(In,Ga)Se₂ monolithic tandem solar cells, *Science* 361 (2018) 904–908.
- [4] Y.C. Liu, et al., Low-temperature-gradient crystallization for multi-inch high-quality perovskite single crystals for record performance photodetectors, *Mater. Today* 22 (2019) 67–75.
- [5] M.I. Saidaminov, et al., Perovskite photodetectors operating in both narrow-band and broadband regimes, *Adv. Mater.* 28 (2016) 8144–8149.
- [6] W.L. Yu, et al., Single crystal hybrid perovskite field-effect transistors, *Nat. Commun.* 9 (2018) 5354.
- [7] C. Xie, et al., Ultrasensitive broadband phototransistors based on perovskite/organic-semiconductor vertical heterojunctions, *Light Sci. Appl.* 6 (2017): e17023.
- [8] F. Li, et al., Ambipolar solution-processed hybrid perovskite phototransistors, *Nat. Commun.* 6 (2015) 8238–8245.
- [9] Q. Zhang, et al., Advances in small perovskite-based lasers, *Small Methods* 1 (2017) 1700163.
- [10] J.Z. Song, et al., Quantum dot light-emitting diodes based on inorganic perovskite cesium lead halides (CsPbX₃), *Adv. Mater.* 27 (2015) 7162.
- [11] B.R. Sutherland, E.H. Sargent, Perovskite photonic sources, *Nat. Photon.* 10 (2016) 295–302.
- [12] N.N. Wang, et al., Perovskite light-emitting diodes based on solution-processed self-organized multiple quantum wells, *Nat. Photon.* 10 (2016) 699–704.
- [13] J. Huang, Y. Shao, Q. Dong, Organometal trihalide perovskite single crystals: a next wave of materials for 25% efficiency photovoltaics and applications beyond? *J. Phys. Chem. Lett.* 6 (2015) 3218–3227.
- [14] Q. Dong, et al., Electron-hole diffusion lengths >175 μm in solution grown CH₃NH₃PbI₃ single crystals, *Science* 347 (2015) 967–970.
- [15] D. Shi, et al., Low trap-state density and long carrier diffusion in organolead trihalide perovskite single crystals, *Science* 347 (2015) 519–522.
- [16] Y.G. Rong, et al., Challenges for commercializing perovskite solar cells, *Science* 361 (2018) 1214–1221.
- [17] D.W. Dequilettes, et al., Impact of microstructure on local carrier lifetime in perovskite solar cells, *Science* 348 (2015) 683–686.

- [18] J. Huang, et al., Understanding the physical properties of hybrid perovskites for photovoltaic applications, *Nat. Rev. Mater.* 2 (2017) 17042.
- [19] J. Chen, N. Park, Causes and solutions of recombination in perovskite solar cells, *Adv. Mater.* (2018) 1803019.
- [20] M. Abdi-Jalebi, et al., Maximizing and stabilizing luminescence from halide perovskites with potassium passivation, *Nature* 555 (2018) 497–504.
- [21] D.Y. Luo, et al., Enhanced photovoltage for inverted planar heterojunction perovskite solar cells, *Science* 360 (2018) 1442–1446.
- [22] K. Zheng, et al., Trap states and their dynamics in organometal halide perovskite nanoparticles and bulk crystals, *J. Phys. Chem. C* 120 (2016) 3077–3084.
- [23] R. Sheng, et al., Photoluminescence characterisations of dynamic aging process of organic-inorganic $\text{CH}_3\text{NH}_3\text{PbBr}_3$ perovskite, *Nanoscale* 8 (2016) 1926–1931.
- [24] A.B. Wong, et al., Growth and anion exchange conversion of $\text{CH}_3\text{NH}_3\text{PbX}_3$ nanorod arrays for light-emitting diodes, *Nano Lett.* 15 (2015) 5519–5524.
- [25] W. Du, et al., Strong exciton-photon coupling and lasing behavior in all-inorganic CsPbBr_3 micro/nanowire fabry-perot cavity, *ACS Photonics* 5 (2017) 2051–2059.
- [26] C. Lin, et al., Giant optical anisotropy of perovskite nanowire array films, *Adv. Funct. Mater.* 30 (2020) 1909275.
- [27] Z. Liu, et al., One-step vapor-phase synthesis and quantum-confined exciton in single-crystal platelets of hybrid halide perovskites, *J. Phys. Chem. Lett.* 10 (2019) 2363–2371.
- [28] Z. Liu, et al., Single-crystal hybrid perovskite platelets on graphene: a mixed-dimensional van der waals heterostructure with strong interface coupling, *Adv. Funct. Mater.* 30 (2020) 1909672.
- [29] S.P. Sarmah, et al., Double charged surface layers in lead halide perovskite crystals, *Nano Lett.* 17 (2017) 2021–2027.
- [30] Z. Yu, et al., Charge transfer effects on resonance-enhanced Raman scattering for molecules adsorbed on single-crystalline perovskite, *ACS Photonics* 5 (2018) 1619–1627.
- [31] W. Peng, et al., Solution-grown monocrystalline hybrid perovskite films for hole-transporter-free solar cells, *Adv. Mater.* 28 (2016) 3383–3390.
- [32] Z.Q. Yang, et al., High-performance single-crystalline perovskite thin-film photodetector, *Adv. Mater.* 30 (2018) 1704333.1–1704333.7.
- [33] Y.X. Chen, et al., General space-confined on-substrate fabrication of thickness-adjustable hybrid perovskite single-crystalline thin films, *J. Am. Chem. Soc.* 138 (2016) 16196–16199.
- [34] Z. Gu, et al., A general printing approach for scalable growth of perovskite single-crystal films, *Sci. Adv.* 4 (2018): eaat2390.
- [35] J. Xing, et al., Dramatically enhanced photoluminescence from femtosecond laser induced micro-/nanostructures on MAPbBr_3 single crystal surface, *Adv. Opt. Mater.* 6 (2018) 1800411.
- [36] M.I. Saidaminov, et al., High-quality bulk hybrid perovskite single crystals within minutes by inverse temperature crystallization, *Nat. Commun.* 6 (2015) 7586.
- [37] T.T. Yin, et al., Hydrogen-bonding evolution during the polymorphic transformations in $\text{CH}_3\text{NH}_3\text{PbBr}_3$: experiment and theory, *Chem. Mater.* 29 (2017) 5974–5981.
- [38] B. Wu, et al., Discerning the surface and bulk recombination kinetics of organic-inorganic halide perovskite single crystals, *Adv. Energy Mater.* 6 (2016) 1600551.
- [39] A.H. Slavney, et al., A bismuth-halide double perovskite with long carrier recombination lifetime for photovoltaic applications, *J. Am. Chem. Soc.* 138 (2016) 2138–2141.
- [40] J.R. Lakowicz, *Principle of Fluorescence Spectroscopy*, Springer, New York, United States, 2006.
- [41] Y. Liu, et al., Temperature-dependent photoluminescence spectra and decay dynamics of MAPbBr_3 and MAPbI_3 thin films, *AIP Adv.* 8 (2018): 095108.
- [42] Z. Zhang, et al., The role of trap-assisted recombination in luminescent properties of organometal halide $\text{CH}_3\text{NH}_3\text{PbBr}_3$ perovskite films and quantum dots, *Sci. Rep.* 6 (2016) 27286.
- [43] S.M. Sze, K.K. Ng, *Physics of Semiconductor Devices*, John Wiley & Sons, New Jersey, United States, 2006.
- [44] H.H. Fang, et al., Ultrahigh sensitivity of methylammonium lead tribromide perovskite single crystals to environmental gases, *Sci. Adv.* 2 (2016): e1600534.
- [45] J.M. Luther, et al., Schottky solar cells based on colloidal nanocrystal films, *Nano Lett.* 8 (2008) 3488–3492.
- [46] K. Tanakaa, et al., Comparative study on the excitons in lead-halide-based perovskite-type crystals $\text{CH}_3\text{NH}_3\text{PbBr}_3$ $\text{CH}_3\text{NH}_3\text{PbI}_3$, *Solid State Commun.* 127 (2003) 619–623.
- [47] G.G. Malliaras, et al., Photovoltaic measurement of the built-in potential in organic light emitting diodes and photodiodes, *J. Appl. Phys.* 84 (1998) 1583–1587.
- [48] R.H. Bube, Trap density determination by space-charge-limited currents, *J. Appl. Phys.* 33 (1962) 1733–1737.
- [49] N.F. Mott, R.W. Gurney, D. J. V., *Electronic processes in ionic crystals*, *J. Chem. Educ.* 42 (1965) A692.
- [50] X. Cui, et al., Temperature-dependent electronic properties of inorganic-organic hybrid halide perovskite ($\text{CH}_3\text{NH}_3\text{PbBr}_3$) single crystal, *Appl. Phys. Lett.* 111 (2017) 233302.
- [51] S.D. Stranks, Nonradiative losses in metal halide perovskites, *Acs Energy Lett* 2 (2017) 1515–1525.
- [52] S.D. Stranks, et al., Recombination kinetics in organic-inorganic perovskites: excitons, free charge, and subgap states, *Phys. Rev. Appl.* 2 (2014): 034007.
- [53] J. Wang, et al., Revealing the properties of defects formed by CH_3NH_2 molecules in organic-inorganic hybrid perovskite MAPbBr_3 , *Appl. Phys. Lett.* 110 (2017) 123903.
- [54] D. Guo, et al., Photoluminescence from radiative surface states and excitons in methylammonium lead bromide perovskites, *J. Phys. Chem. Lett.* 8 (2017) 4258–4263.